Extending the performance limit of anodes: insights from diffusion kinetics of alloying anodes

Yong-Seok Choi,[1,2,3] David O. Scanlon,[1,2,3,4] and Jae-Chul Lee[5,*]

[1] Department of Chemistry, University College London, 20 Gordon Street, London WC1H 0AJ, UK
[2] Thomas Young Centre, University College London, Gower Street, London WC1E 6BT, UK
[3]The Faraday Institution, Harwell Campus, Didcot OX11 0RA, UK
[4]Diamond Light Source Ltd., Diamond House, Harwell Science and Innovation Campus, Didcot, Oxfordshire OX11 0DE, UK
[5] Department of Materials Science and Engineering, Korea University, Seoul, 02841, South Korea

Abstract: Alloying anodes have long been attracting attention as promising candidate electrodes for application in grid-level energy storage systems owing to their high energy capacity. Alloying anode-based batteries, however, remain far from practical applications, which require several issues affecting cell performance to be addressed. The large volumetric expansion of anodes and associated phenomena occurring during battery cycling are the main reasons for the poor electrochemical performance of alloying anodes. These electrochemical behaviors of alloying anodes originate from the reactions between the unreacted anode material and inflowing carrier ions. Thus, the diffusion kinetics plays a key role in determining the electrochemical properties of alloying anodes. Recent advances in analytical instruments and atomic simulations offer new approaches for interpreting anode performance. Beginning with a brief historical background, this review presents an overview of the origin of diffusion kinetics and how this concept has been extended to alloying anodes. Accordingly, the relationship between the diffusion kinetics and

electrochemical performance of alloying anodes is discussed, combined with efficient strategies that can be adopted to improve electrochemical properties. Finally, we propose a design overview of next-generation alloying anodes that can extend the batteries' performance limit.

Keywords: rechargeable battery, alloying anodes, diffusion kinetics, anisotropic swelling, self-limiting diffusion.

*To whom correspondence should be addressed. Jae-Chul Lee (email: jclee001@korea.ac.kr)

1. Introduction

Since the first commercialization of lithium-ion batteries (LIBs) in the early 1990s [1], LIBs, in conjunction with transition metal oxide cathodes [2, 3] and carbonaceous anodes, have been attracting considerable attention as advanced energy storage devices [4]. The current success of LIBs is primarily attributed to the insertion mechanism of Li ions that occurs between the layers of host electrodes [5, 6]. This mechanism allows electrodes to operate without significant structural changes for prolonged periods and enables LIBs to exhibit a long cycle life, high stability, and moderate energy capacity that are close to their theoretical limits (Figure 1) [3, 7-16]. However, with the rapid expansion in the capacity demands of electric vehicles and grid-scale energy storage systems, current electrodes based on the insertion mechanism are being criticized for their limited energy density.

In a continuous effort by the research community to develop high-performance rechargeable batteries, electrode materials that follow alternative mechanisms have been investigated [17]. Electrochemical processes involving conversion and alloying mechanisms exhibit much greater theoretical capacities than those of processes based on the insertion mechanism, thus enabling the realization of high-energy-density electrodes for next-generation batteries (Figure 1). The high theoretical capacity of conversion and alloying electrodes originates from their unique uptake mechanisms of carrier ions; unlike insertion electrodes, conversion and alloying electrodes accommodate carrier ions by disrupting the crystal structure of host electrodes. This allows a large number of carrier ions to be stored without the restraint of the crystal frameworks of electrodes, which is particularly true for alloying anodes; Si, for example, can accept Li ions up to 4.4 per unit formula and yield a theoretical capacity of 4200 $mAhg^{-1}$ (Figure 1a). However, the alloying of Si with Li inevitably causes large volumetric changes in the Si anodes during electrochemical cycling

[18, 19], resulting in performance issues associated with the mechanical degradation of Si, such as a short cycling life and low practical capacity.

The increasing knowledge gap between the degradation process and changes in the electrochemical properties of alloying anodes has motivated various theories and experiments on the diffusion kinetics of alloying anodes [11-15, 17]. Accumulated models and experimental evidence reveal that carrier ions are diffused into alloying anodes by forming an intermediate reaction layer that separates the unreacted alloying anodes from inflowing carrier ions. This diffusion process, often referred to as two-phase reaction/diffusion, means that the overall diffusion rate is governed either by the diffusion rate of charge carriers at the propagating phase boundary (v_i) or that at bulk regions (v_b) of the trailing intermediate reaction layer (Figures 1b) [20]. The former mode of diffusion is termed an interface-controlled reaction (ICR), whereas the latter is called a diffusion-controlled reaction (DCR) [21]. Although various electrochemical properties of alloying anodes are closely related to their diffusion kinetics, their relationship remains largely unexplained because of a lack of appropriate characterization of the atomic structures of the materials present. In the past decade, there has been significant progress in nanotechnology and atomic simulations that has enabled exploring the diffusional behaviors (e.g., orientation-dependent diffusion, diffusion rate, and penetration depth of carrier ions) in alloying anodes and their effect on anode performance. In this regard, an in-depth understanding of the diffusion kinetics of alloying anodes can offer a rational strategy for the design and architecture of advanced anode materials with enhanced properties.

This progress report, mainly from the perspective of diffusion kinetics, aims to understand the origin of the electrochemical behaviors of alloying anodes and address their poor electrochemical performance (i.e., cycle life, rate performance, and practical capacity). First, we

summarize the research history of diffusion kinetics and its extension to alloying anodes. Additionally, three sections successively discuss details on the electrochemical performance of alloying anodes and their relationship with diffusion kinetics. Finally, on the basis of this relationship, we clarify two important material properties, i.e., bond strength and yield strength, for determining anode performance, which can be used as material design principles for developing future batteries with superior electrochemical performance.

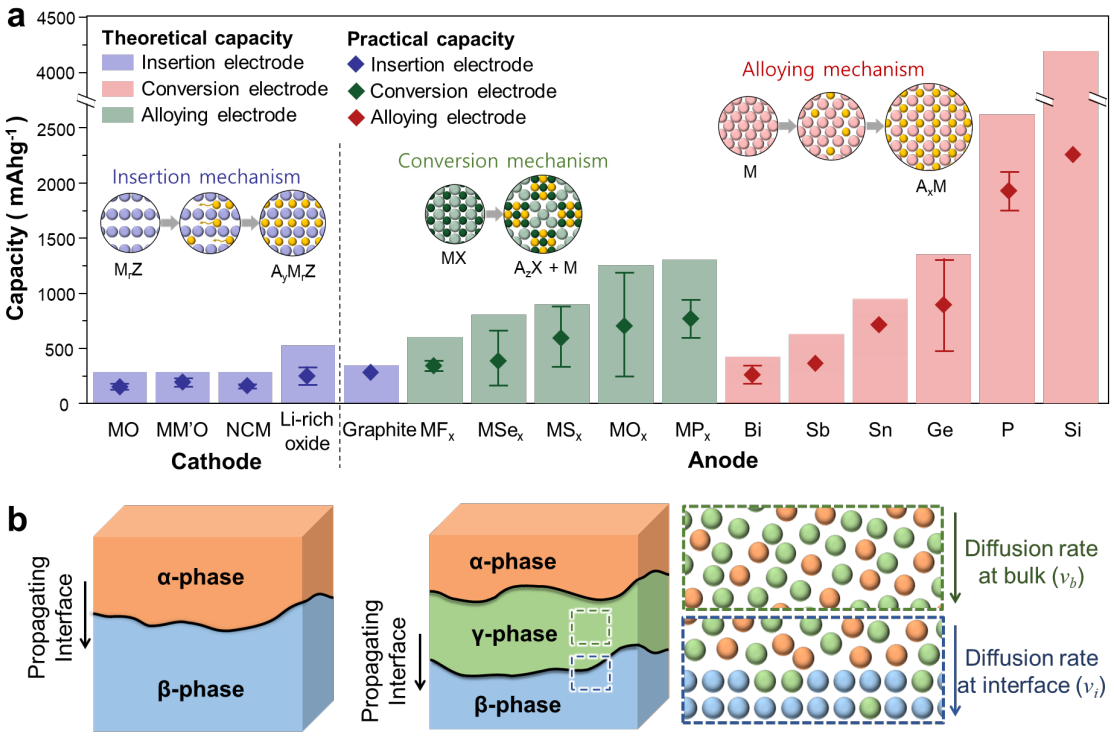

Figure 1. (a) Comparison of the theoretical (colored bars) and practical (◆) capacities of cathode [3,7,8] and anode [9-16] materials governed by different diffusion mechanisms. The practical capacities are obtained by averaging the specific capacities of Li half cells measured after 20 cycles. The error bars indicate the maximum and minimum values of the capacities reported for each electrode. (b) Schematic of a diffusion couple showing that the diffusion in alloying anodes proceeds by forming an intermediate reaction layer that allows the diffusion to occur via the two-phase reaction.

2. Research history of diffusion kinetics

2.1. Early studies on diffusion kinetics

Studies on diffusion kinetics were initially triggered by the need to control the oxidation behavior of metals. An oxide layer, when growing slowly by adhering to the metal surface, can act as a passive layer that can protect the metal from further oxidation. Conversely, loose, fast-growing oxide layers tend to degrade substrate metals, causing them to fail after prolonged use. For engineering design, therefore, an understanding of the oxidation rate is an important task in estimating the lifespan of metals, and this requirement motivated various experiments aiming to measure the oxidation rate of metals in the early 1920s. Based on accumulated experimental data, Wagner established the diffusion kinetics by relating the oxide layer thickness (L) and oxidation time (t) by the $L^2 \propto t$ law (also called the parabolic rate law and later termed DCR) [22, 23]. This parabolic relation is obtained because the oxidation rate at the propagating phase boundary (or interface) is faster than that in trailing bulk oxide regions; consequently, the overall diffusion rate is governed by the reactions in the trailing bulk regions. In addition to the parabolic rate law, the linear rate law of $L \propto t$ occurs when the diffusion rate of solute atoms is faster at the trailing reaction layer than that at the propagating phase boundary or interface. This linear relation is obtained because the overall diffusion rate is limited by the reactions at the interface, which are called ICR [24, 25].

The concepts of ICR and DCR were actively discussed for conventional alloys in the late 20th century to explain the relationship between the diffusion kinetics and the reactions that limit the overall diffusion rate in conventional alloys. Experiments reported in this period [26-28] were mainly on DCR diffusion (Figure 2a) and analyzed using various numerical models for solid-state diffusion. Large-scale simulation based on finite element method (FEM) analysis is probably the most common method used to analyze the local compositions and respective stress states under a

given diffusion kinetics. Murray et al. developed a generic computational model for the solid-state diffusion of systems governed by DCR [29]. This finite element (FE) model assumes the local equilibrium state at the phase boundary and allows the prediction of the position of the moving phase boundary as a function of time; this model was later used as a basis for calculating local stresses near the propagating interface [30].

The DCR diffusion model was subsequently extended to ICR diffusion by considering the non-equilibrium condition at the phase boundary; then, it was used to evaluate various parameters affecting diffusion behaviors [31]. In the 2000s, with the development of advanced analytical instruments, the direct observation of moving phase boundaries became feasible, enabling detailed studies on the diffusion kinetics and associated changes in microstructures. In-situ experiments performed to measure the thickness of the reaction layer at the interface confirmed that the $L \propto t$ law and orientation-dependent diffusion are valid for systems governed by ICR (Figure 2b) [32, 33]. Based on these observations, Jeffrey et al. speculated that ICR can be responsible for the anisotropic diffusion, often observed in the Li-Si system [34].

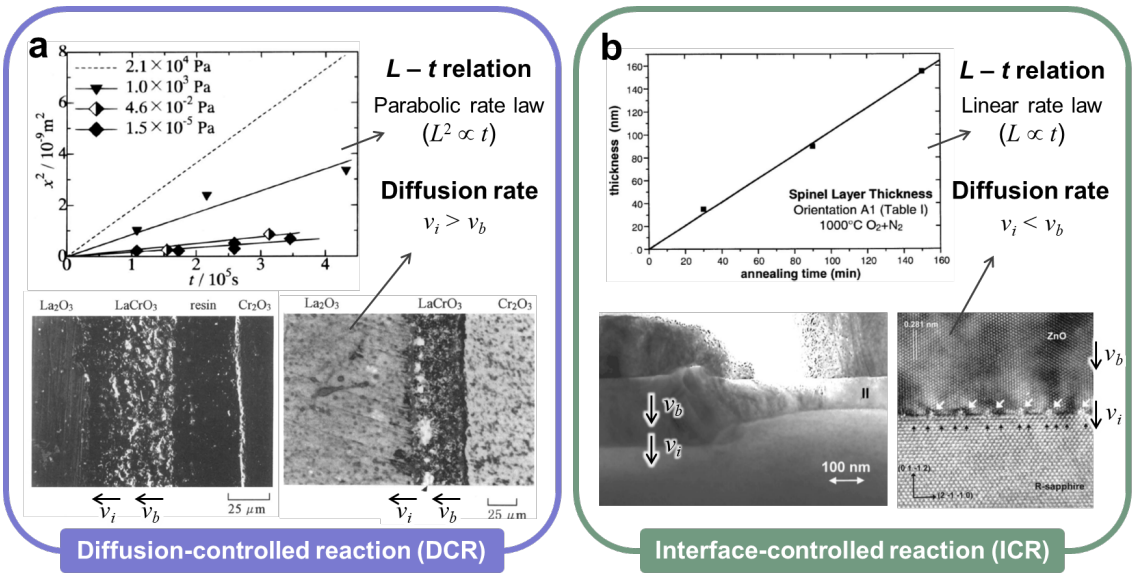

Figure 2. Representative works on the diffusion behaviors governed by (a) DCR [35] and (b) ICR [32]. The systems governed by DCR and ICR are characterized by the $L^2 \propto t$ and $L \propto t$ laws, respectively. Reproduced with permission from Refs. [32, 35] Copyright © 1998 IOP publishing and © 2000 AIP publishing LLC.

2.2. Extension of theories on diffusion kinetics to alloying anodes

Although theories on diffusion kinetics were introduced for conventional alloys in the early 1920s, it was not until the 2010s when researchers began to adopt these theories to explore various diffusion behaviors occurring in alloying anodes. Huang *et al.* developed the first open-cell micro-electrochemical device that can be mounted inside an in-situ transmission electron microscopy (TEM) instrument [36] and observed the microstructural evolution of Si nanowires (NWs) during Li diffusion [19]. They observed that the Li diffusion in Si NWs proceeds by forming an amorphous Li_xSi layer, thereby establishing two-phase diffusion. Experiments show that the propagation length (L) of the interface is linearly related to the diffusion time (t), suggesting that the lithiation of crystalline Si is governed by ICR. This $L \propto t$ relation arises from short-range diffusion occurring at atomically sharp interfaces with a thickness of ~1 nm [18]. This suggests that the Li diffusion at the interface is too slow to transport Li ions to regions away from the interface, causing the entire diffusion to be governed by ICR. Furthermore, the short-range diffusion occurring at the interface causes the Li diffusion rate to differ depending on the orientation of the crystalline Si, rendering the volume change of the lithiated Si NWs highly anisotropic [37].

Because lithiation behaviors are directly influenced by the nature of the Si/Li_xSi interface, model studies were performed to evaluate the physics underlying the lithiation of Si. In early model studies on the Li/Si diffusion couple, researchers commonly assumed the lithiation rate of Si to be

limited by the diffusion rate at the trailing Li_xSi region (i.e., DCR), while ignoring the orientation-dependent diffusion of the advancing interface [38, 39] and thus failed to reproduce the sharp Si/Li_xSi interface and abrupt changes in the Li composition observed in experiments. To predict the abrupt changes in the composition and the associated development of residual stresses at the Si/Li_xSi interface, new models were created by assuming the lithiation rate of Si NWs to be limited by ICR diffusion. Models based on ICR diffusion could not only explain the crack formation behaviors of Si particles during lithiation [40] but also reproduce anisotropic morphologies of lithiated Si NWs [37]. Another important finding observed from Li/Si systems is that ICR diffusion is influenced by various material characteristics, such as the molar volume of Si, Li diffusivity in Li_xSi, radius of Si particles, and rate constants for the reaction toward Si [20]. These results obtained from Li/Si systems explain why Si anodes exhibit abrupt changes in the Li composition profiles [37, 40], high residual stresses [20], anisotropic swelling [37], and associated crack formation [40], which are closely related to such anodes' electrochemical performance.

Studies on alloying anodes governed by DCR diffusion began only in the late 2010s. Ironically, the first reported case of DCR diffusion is also the lithiation of crystalline Si. Seo at al. performed direct-contact lithiation experiments using Si NWs with a diameter of ~80 nm [41]. They observed that the propagation length (L) of the reaction front changes with time (t) according to the $L^2 \propto t$ relation, indicating that the lithiation of the 80-nm-thick Si NWs follows DCR. On the other hand, the lithiation of Si NWs with diameters greater than 100 nm follows ICR [19, 42]. The contradictory results obtained from the above experiments indicate that the diameter/size of anode materials is another parameter affecting the diffusion kinetics of alloying anodes. Notably, the transition in diffusion kinetics from ICR to DCR significantly improves the Li diffusion rate in Si NWs; the propagation speed of the lithiation front measured from the 80-nm-diameter Si NWs was

179 1082 nm s^{-1} [41], which is nearly three orders of magnitude greater than that measured for 140-nm-
180 diameter Si NWs (1.7 nm s^{-1}) [43]. In addition to Li/Si systems, DCR diffusion was observed to
181 occur in Na/Sn [44], Li/Ge [45], and Na/Ge [46] systems. Contrary to systems governed by ICR,
182 systems following DCR diffusion commonly display 1) comparatively fast diffusion rates, 2)
183 isotropic swelling or expansion, and 3) deep penetration depths of carrier ions. All these behaviors
184 are desirable for improving the electrochemical properties of alloying anodes, as typically revealed
185 by charge rate, cycle life, and energy capacity. Therefore, diffusion kinetics and its effects on
186 anode performance should be understood to extend/break the performance limit of conventional
187 alloying anodes. This point is elaborated in the following section by relating diffusion kinetics
188 with the abovementioned diffusion behaviors.
189

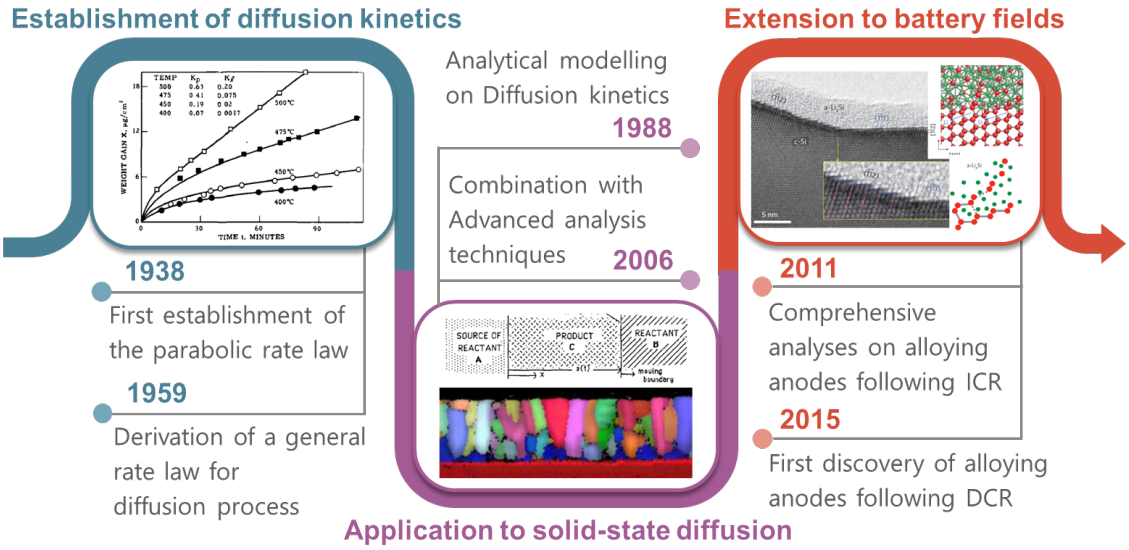

190

191 **Figure 3.** Schematic of the research history of diffusion kinetics, showing the establishment of the
192 theories on diffusion kinetics and its recent application to alloying anodes [34, 42, 47].
193

194 **3. Relationship between diffusion kinetics and anode performance**

195 Lack of capacity retention, slow charging rate, and short cycling life, which are directly
196 related to the diffusion mechanisms operating in alloying anodes, are the major challenges that
197 limit the commercialization of such anodes. Considerable effort has been exerted to address these
198 issues in both LIBs [48] and Na-ion batteries (NIBs) [49]. Of the various morphologies of anode
199 materials, samples in the form of NWs are the most common shapes for analyzing the related
200 diffusion kinetics because of two reasons. (1) One-dimensional NWs allow the direct tracking of
201 the moving interface and associated analyses of the L vs. t relation. (2) Compared with film- or
202 particle-type anodes, NW-shaped anodes accumulate comparatively low residual stresses during
203 battery cycling. Anode samples with low residual stresses are particularly important for studying
204 the diffusion kinetics intrinsic to anode materials because residual stresses can change the shape
205 of the L vs. t curve and cause a system to seem governed by different diffusion kinetics. For
206 example, in a Si particle, the shape of the L vs. t curve associated with lithiation is greatly affected
207 by residual stresses whose magnitude is inversely proportional to the particle diameter; in principle,
208 the lithiation of Si is governed by ICR and should exhibit the $L \propto t$ relation during lithiation
209 (Section 2.2). However, the lithiation of Si particles appears to follow the parabolic rate law ($L^2 \propto$
210 t) because of the residual stresses accumulated at the Si/Li_xSi interface in particle-shaped Si anodes
211 [50]. Therefore, cylindrical anode materials should be used to minimize the residual stresses
212 developed at the interface and eliminate the associated artifacts. For this reason, this review is
213 mainly conducted from the perspective of NW-shaped alloying anodes and summarizes how their
214 diffusion behaviors and corresponding diffusion kinetics are related to such anodes'
215 electrochemical properties, such as cycle life, rate performance, and specific capacity.
216

3.1. Diffusional anisotropy and cycle life of anodes

The structure of anodes suffers from continual degradation during battery cycling, which reduces the cycle life of the anodes. Of the various factors affecting the structural degradation of anodes, orientation-dependent volume expansion is the most detrimental. For alloying anodes, especially those following ICR diffusion, the difference in volume expansion can differ by up to ~400%, depending on the crystallographic orientation. This variation causes the alloying anodes to swell anisotropically. Large anisotropic swelling induces inhomogeneous stresses in alloying anodes, which in turn cause mechanical degradation, as revealed by crack formation and anode pulverization [19, 51]. Because the anisotropic swelling behavior of anodes is closely related to the diffusion kinetics of anode materials, we compare the degree of anisotropic swelling of anodes governed by different diffusion kinetics and assess the relationship between the diffusion kinetics and cyclability of alloying anodes.

Systems governed by ICR: Until the early 2000s, anisotropic solid-state diffusion was known to occur only for materials with a non-cubic crystal symmetry. This is because, for systems defined in continuum theory, the properties of crystals with a cubic symmetry are characterized by a zero-rank tensor (i.e., scalar value) and thus are isotropic [52]. However, the model based on continuum theory was found to no longer hold for the diffusion behaviors of alloying anodes. The best example that violates the conventional rule is the anisotropic swelling of crystalline Si with a diamond cubic symmetry [19, 37]; observations of lithiated Si NWs revealed anomalous volume changes wherein the shape of fully lithiated Si NWs differs depending on the crystallographic orientations of the NWs (Figure 4a) [19, 37]. Subsequent TEM analyses were performed on a Si/Li_xSi interface to understand the physics underlying these observed anisotropic swelling behaviors

(Figure 4b). Observations of lithiated Si NWs revealed that the Si/Li_xSi interface is atomically sharp and thin [18] and propagates toward unreacted Si by defoliating close-packed Si (111) planes [42]. This defoliation, which is associated with the orientation-dependent, short-range diffusion near the interface, causes the propagation speed of the interface to differ according to the crystallographic orientation, resulting in anisotropic swelling.

The above discovery on the ICR diffusion of Li/Si systems facilitated computational studies on the reactions occurring at the Si/Li_xSi interface. On the basis of this observed defoliation phenomenon, Liu et al. established an elasto-plastic deformation model and showed that the anisotropic lithiation of Si NWs is attributed to the orientation of Si NWs at the Si/Li_xSi interface [42]. Furthermore, the measurements of the propagation speed of the interface enable predicting the morphological changes of Si NWs during lithiation. Using measured lithiation rates, an FEM study calculated the Li diffusivity at the Si/Li_xSi interface, followed by a simulation of anisotropic swelling and crack formation (Figure 4c) [53]. To further understand the reactions occurring at the interface, atomic simulations based on molecular dynamics (MD) were performed to elucidate the changes in atomic structures and stress states at the Si/Li_xSi interface during lithiation. This approach allowed the validation of the previously reported defoliation behaviors of Si (111) planes while assessing residual stresses and their effect on the anisotropic diffusion behavior (Figure 4d) [54, 55]. Recent works on the diffusion energy barrier at the Si/Li_xSi interface show that anisotropic diffusion may arise from the orientation-dependent thermodynamic stability of the Si/Li_xSi interface rather than from diffusion barriers for Li diffusion across the interface [56, 57]. Despite this unsettled debate, subsequent density functional theory (DFT) calculations further elaborated the computational results by revealing the preferential pathways for Li diffusion and associated diffusion barriers; Li ions tend to migrate along a direction parallel to the Li concentration gradient

263 by taking regions or spaces with low valence electrons [58-60]. According to this simulation study,
264 the tortuosity of diffusion pathways is the structural origin of the anisotropic Li diffusion behavior
265 [61].

266 Analyses of the anisotropic swelling behavior of Si NWs triggered extensive studies on the
267 anisotropic diffusion of other alloying anodes. In-situ TEM observations on the lithiation behaviors
268 of black phosphorus (P) show that the transformation from orthorhombic P to amorphous Li_xP is
269 accompanied by a large anisotropic volume expansion and associated crack formation (Figure 4e)
270 [62]. Similar results are observed when Li is substituted with Na; during sodiation, crystalline P
271 expands preferentially along the [010] direction (Figure 4f) [63, 64]. In addition to crystalline P, Sb
272 also expands anisotropically upon sodiation [51]. All these systems follow the $L \propto t$ relation during
273 lithiation/sodiation. Thus, ICR diffusion is characterized by short-range diffusion and strongly
274 correlated with diffusional anisotropy.
275

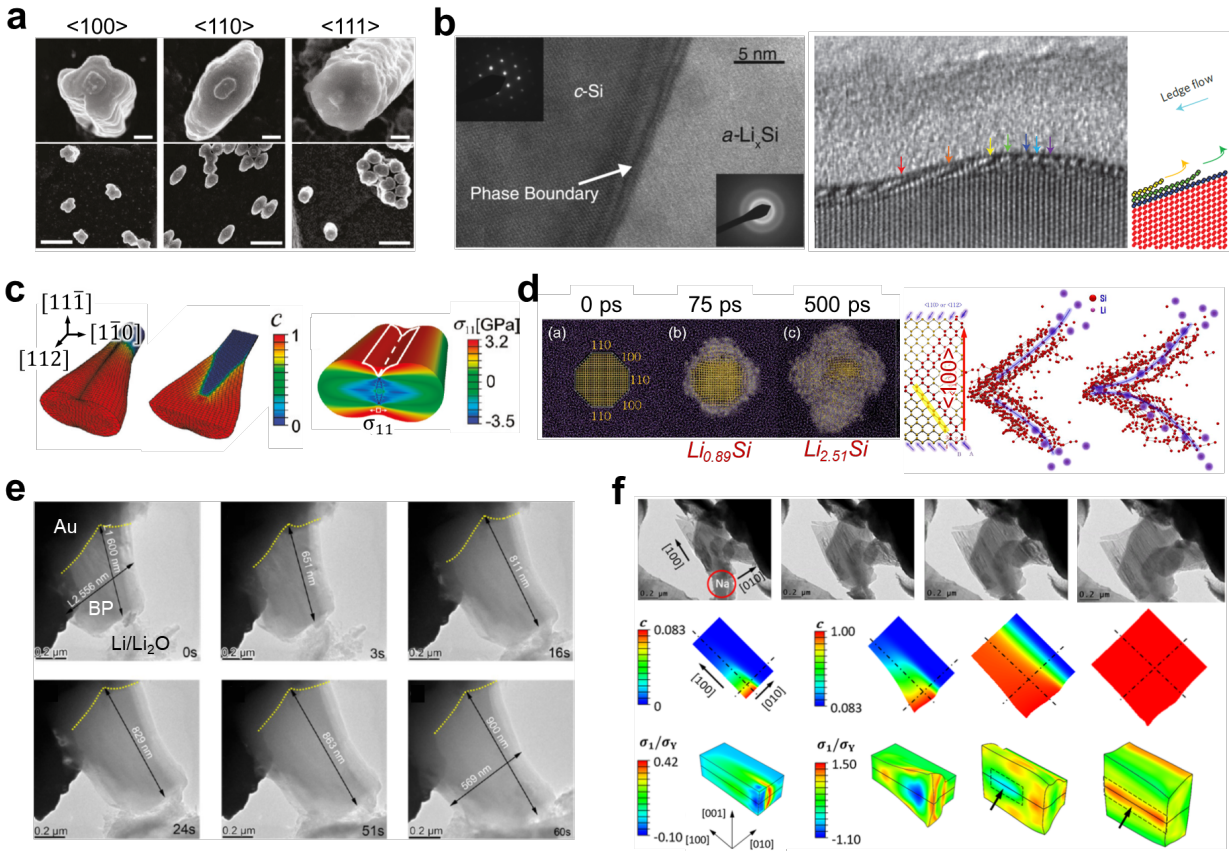

Figure 4. (a) SEM images of Si NWs subjected to lithiation, showing different morphological changes depending on the initial crystallographic orientation of the Si NWs [37]. (b) High-resolution TEM images of the atomically sharp interface between crystalline Si and lithiated Li_xSi [18, 42], showing the defoliation of close-packed Si (111) planes. (c) FEM simulation results on the distribution of Li contents and residual stresses in the lithiated Si NWs [19]. (d) MD simulations showing the morphological evolution of Si NWs associated with the lithiation [54]. (e) SEM images of black P undergoing anisotropic swelling during lithiation [62]. (f) SEM images and FE analysis on a partially sodiated P particle, showing the distribution of the Na contents and associated residual stresses [64].

Systems governed by DCR: For systems governed by DCR diffusion, the overall diffusion

288 rate is limited by the diffusion of carrier ions in the trailing bulk region rather than by the diffusion
289 at the interface. Consequently, the overall diffusion rate and associated swelling behaviors no
290 longer depend on the crystallographic orientation of the anode material at the interface. Therefore,
291 contrary to alloying anodes governed by ICR, those governed by DCR display an isotropic volume
292 expansion during battery cycling. For example, the sodiation of 500-nm-diameter Sn NWs expands
293 at equal rates along the radial direction regardless of the crystallographic orientations, resulting in
294 isotropic swelling (Figure 5a) [65]. Measurements of the propagating speed of the interface reveal
295 that the interface advances by following the $L^2 \propto t$ relation, which confirms that the diffusion of
296 Na into crystalline Sn is governed by DCR. The sodiation and lithiation behaviors of Ge NWs also
297 follow the $L^2 \propto t$ law [45, 46], thus causing Ge NWs to expand in a nearly isotropic manner. These
298 results obtained from Ge NWs suggest that DCR diffusion is valid for such systems.

299 Notably, the crystal structures of anode materials following DCR diffusion have little in
300 common: Sn (body-centered tetragonal) and Ge (diamond cubic). This suggests that the diffusion
301 behaviors of anode materials following DCR are less likely to be affected by their crystal structure
302 and orientation. Therefore, structural changes other than orientation effects are responsible for
303 DCR diffusion. In early studies on the isotropic swelling of lithiated Ge NWs, this behavior was
304 initially interpreted by relating the lithiation rate to the etching rate during wet-etching experiments
305 [45]. Experiments showed that, compared with the etching rate of Si, that of Ge was approximately
306 isotropic [66, 67]. This indirectly indicated that the mobility of the lithiated Ge region is less sensitive
307 to the orientation of the crystalline Ge. Although this explanation provided insights for
308 understanding the isotropic diffusion behavior associated with DCR, it lacked a theoretical basis
309 to support the DCR diffusion occurring during the two-phase reaction.

310 To further elucidate the structural origin of DCR diffusion, DFT calculations were performed

on a Na/Sn diffusion couple while observing the structural evolution of crystalline Sn adjacent to the interface formed during sodiation. Calculations showed that, as Na ions begin to inflow into the crystalline Sn, the crystal structure of the Sn near the interface becomes prone to disruption, forming a thin layer of an amorphous phase (Figure 5c) [44, 65, 68]. The structure of thus-formed amorphous layer near the interface is similar regardless of the initial orientation of crystalline Sn; this weakens or nullifies the directionality of Na diffusion and promotes isotropic diffusion. These results indicate that isotropic diffusion can readily occur for alloying anodes with lower interatomic bond energies. Therefore, such materials would require less energy to disrupt their initial crystalline structures and thus facilitate amorphization behaviors. As explained in detail in Section 3.2, the amorphization at the interface is an important structural origin that not only causes isotropic diffusion but also accelerates the diffusion of carrier ions. This renders the overall diffusion rate to be controlled by the trailing bulk region, i.e., DCR diffusion.

In addition to low bond energies, the diameter of NWs can promote the formation of amorphous phases in front of the advancing interface and the associated isotropic diffusion. For instance, a previous study on the oxidation behavior of Si NWs reported that the pristine Si core does not act as a rigid mechanical constraint during oxidation when the diameter of Si NWs is smaller than 5 nm [69]. As a result, for small Si NWs, the crystalline structures of the Si core can be readily disrupted to reduce residual stresses during oxidation (Figure 5d). This behavior of amorphization weakens the orientation-dependent diffusion in Si NWs, thus enabling the oxidation to proceed in an isotropic manner. Amorphization behaviors similar to Si are observed from various metal NWs, whereas their threshold diameter for promoting the amorphization behavior differs depending on the materials [70]: 300 nm for Si [37, 71], 1200 nm for Ge [72], and ~60 nm for CuO [73].

The above experimental and simulation results suggest that, in principle, DCR diffusion and the associated isotropic swelling are feasible for group IVA and VA elements with small diameters and interatomic bond energies. Considering that isotropic swelling can prevent the accumulation of high residual stresses and crack formation [70], the cyclability of alloying anodes could be improved by decreasing their size to below the threshold diameter. However, the synthesis of nanoscale anode materials is challenging and costly because of their susceptibility to external contaminants, such as oxygen and moisture [74]. Therefore, given the cost and complexity of anode fabrication, alloying anodes with large threshold diameters are desirable for producing long-lasting alloying anodes.

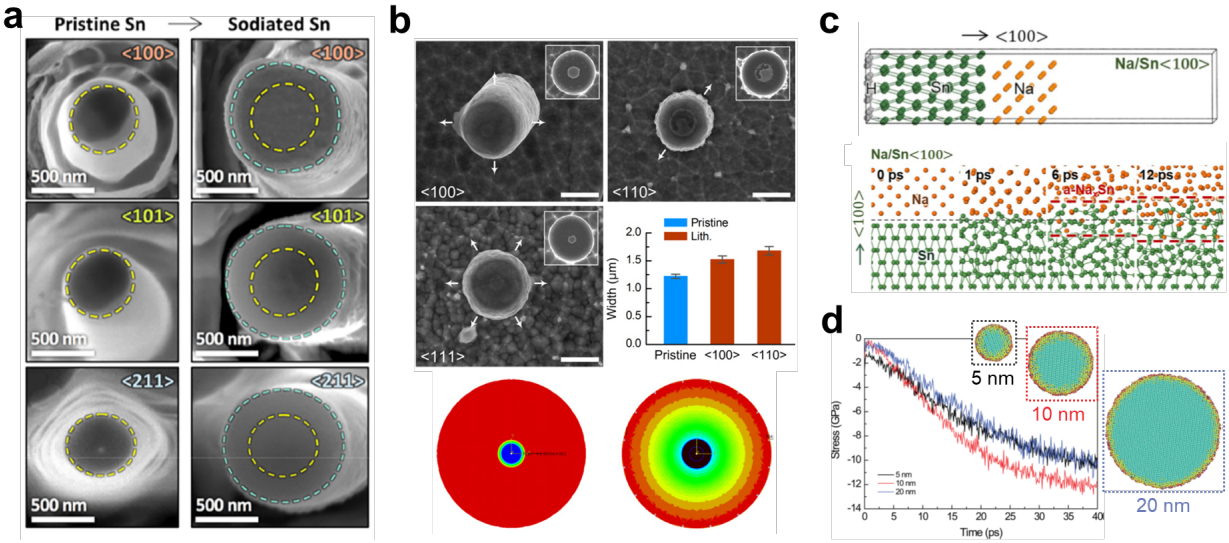

Figure 5. SEM images of the (a) sodiated Sn [65] and (b) lithiated Ge NWs [72], showing that these materials expand isotropically regardless of their crystallographic orientation during sodiation/lithiation. (c) DFT calculations performed on the Na/Sn diffusion couple, displaying that sodiation of Sn proceeds by the formation of a thin amorphous Sn layer in front of the advancing interface [44]. (d) Distribution of residual stresses of partially oxidized Si NWs, showing the release of residual stresses in Si NWs with diameters smaller than 5 nm [69].

351

352 **3.2. Diffusion rate of carrier ions and rate performance**

353 Compared with insertion electrodes, alloying anodes display slow diffusion rates of carrier
354 ions; thus, batteries exhibit poor rate performance. Reduced diffusion rates within alloying anodes
355 arise from the characteristic diffusion mechanism of carrier ions operative in these anode materials.
356 The width of diffusion channels, where carrier ions can diffuse, is not large in alloying anodes,
357 unlike that in insertion electrodes. Hence, the carrier ions within alloying anodes diffuse by
358 breaking the atomic bonds of the host anode material, leading to the disruption of the crystal
359 structures. This process requires additional energy and thus significantly lowers the diffusion rate
360 of carrier ions. Therefore, the disruption process of the crystal structure of anode materials needs
361 to be analyzed to understand the diffusion rate and associated rate performance of alloying anodes.
362 In this section, the structural changes occurring in alloying anodes are compared for systems
363 following ICR and DCR diffusion, and the relationship between the diffusion mechanism and
364 diffusion rate of carrier ions is discussed.

365

366 **Systems governed by ICR**: Previous studies on diffusion in alloying anodes found that
367 systems such as Li/P [62], Na/Sb [44], and Li/Si [19] are controlled by ICR (Figure 6a). For these
368 systems, the diffusion rate is governed by the diffusion of carrier ions at the propagating interface,
369 resulting in low diffusion rates of carrier ions. In general, this characteristic diffusion is related to
370 the two structural features of the propagating interface, i.e., 1) the atomically sharp/narrow
371 interface [75, 76] and 2) the curvature of the interface [40, 50, 75].

372 The presence of an atomically sharp interface in ICR-governed systems implies that the
373 composition of carrier ions changes rapidly across the interface. This change in the composition

induces a large misfit strain and develops high compressive residual stresses to the unreacted anode material near the interface [18]. Compressive residual stresses (σ) in turn increase the activation energy (or diffusion barrier) for diffusion by a certain amount ($\sigma\Delta V$), which reduces the diffusivity and hinders the additional inflow of carrier ions into the anode. This is often revealed in experiments as a phenomenon called the "self-limiting diffusion" behavior [77-79] and is explained in detail in Section 3.3. One way to mitigate the formation of a sharp interface is to utilize anodes with amorphous phases. For example, compared with crystalline Si with a sharp interface, an amorphous structure with a broad interface can transport Li ions into the Si anode at faster rates. This is because amorphous Si is characterized by loosely packed atomic structures (of Voronoi polyhedral [80]) and thus can readily transport Li ions through an amorphic interface (Figure 6b).

Another important parameter that limits the diffusion rates of alloying anodes is the curvature of the propagating interface. Compared with a flat/straight interface, a curved interface develops additional compressive stresses in the direction tangent to the interface during the diffusion of carrier ions. The increment in stress is linearly related to the curvature (or inversely proportional to the radius) of the interface, thereby reducing the diffusion rates of carrier ions at the interface. A subsequent model study quantified this decrease in the diffusion rate by relating the residual stress at the interface with the increase in Gibbs free energy [40]. This model was later used to analyze the residual stresses generated within Si particles during lithiation and the corresponding changes in the lithiation rate (Figure 6c) [50], and the results were subsequently validated through experiments [81].

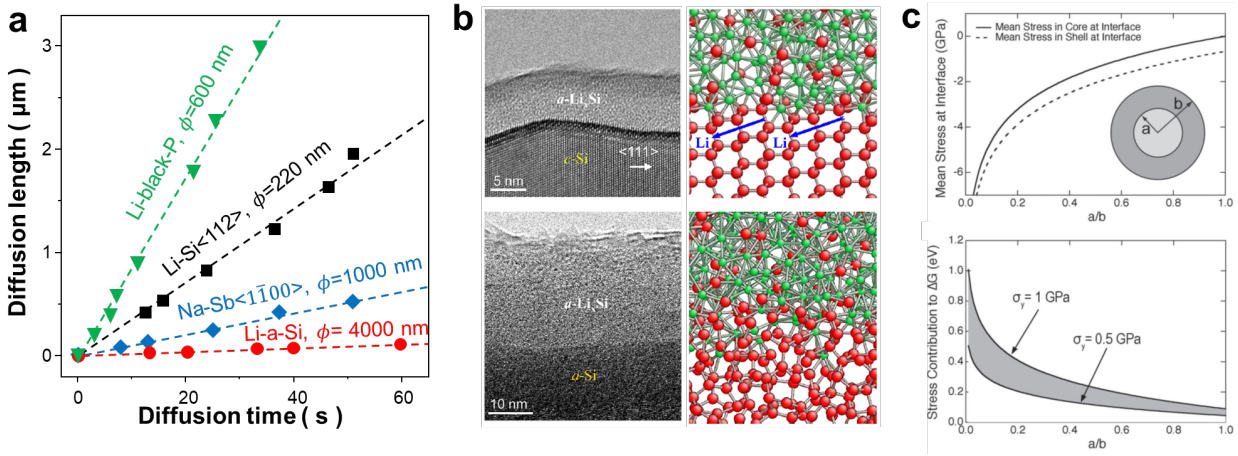

Figure 6. (a) The L vs. t graphs constructed for various alloying anodes following ICR [19, 44, 62, 76]. (b) TEM images and MD simulation results, showing different interfacial structures observed from crystalline and amorphous Si subjected to lithiation [76]. (c) Changes in the residual stress and the corresponding changes in Gibbs free energy calculated as a function of lithiated layer thickness in the Si particle [50].

Systems governed by DCR: With the progress of researches on alloying anodes, alloying anodes that cannot be explained by the ICR diffusion mechanism were discovered for the Na-Sn [82] and Li-Ge [45] systems. These systems commonly follow the $L^2 \propto t$ law in solid-state diffusion (Figure 7a), whereas the propagation rates of the interface were faster by 2–3 orders of magnitude than those of alloying anodes following ICR diffusion (Figures 6a and 7a). The $L^2 \propto t$ relationship and fast diffusion rates of carrier ions suggest that the diffusion of carrier ions in these systems is not restricted by the propagating interface, a characteristic of the DCR diffusion mechanism.

Huang et al. [36] performed direct-contact in-situ lithiation experiments on SnO_2 NWs and observed that DCR diffusion arises from the formation of an amorphous phase and dislocation cloud near the propagating interface during Li diffusion (Figure 7b). Such structural changes,

412 especially dislocation generation, are induced because of the initial preference of Li diffusion
413 along the [001] direction of SnO_2, which causes a ~10% lattice expansion in the (100) planes [83].
414 These dislocations and amorphous phases act as fast diffusion pathways of Li ions [84] and thus can
415 carry Li ions to regions away from the interface, thereby enabling long-range diffusion, which is
416 a characteristic of DCR. The formation of dislocation clouds and the long-range diffusion behavior
417 of carrier ions are also observed from other oxide anode materials, such as ZnO [85] and RuO_2 [86].

418 Theories explaining ICR diffusion can be extended to explain the diffusion behaviors of
419 alloying anodes following DCR diffusion. For a Na/Sn system, the propagation length (L) of the
420 interface measured from Sn NWs follows the $L^2 \propto t$ law, suggesting that the sodiation of Sn is
421 governed by DCR (Figure 7a). Compared with systems following ICR, systems following DCR
422 commonly exhibit a high diffusivity of carrier ions and thus improved rate performance. The
423 enhanced diffusivity measured from DCR-governed anode materials arises from two different
424 structural features: the formation of a thin amorphous layer and dislocations in front of the
425 interface. Byeon et al. performed ab initio MD simulations on a Na/Sn system to quantitatively
426 explain how the amorphization can promote the diffusivity of carrier ions in the system following
427 DCR [65, 68]. Calculations showed that the amorphization increases the interatomic bond distance
428 of the adjacent Sn−Sn pairs near the interface (Figure 7c). Therefore, the amorphization at the
429 interface causes the phase to reveal atomically open spaces. These spaces provide a preferential
430 passage for Na diffusion and thus facilitate the fast transport of Na ions at the interfacial region.
431 When viewed at the macroscopic scale, the amorphization at the interface alleviates the rate-
432 limiting behavior of the propagating interface and causes the overall kinetics of the system to
433 follow DCR diffusion. Additional advanced analyses performed at the propagating interface reveal
434 that dislocations formed within crystalline Sn act as preferential pathways for Na diffusion (Figure

7c) [65].

Both the amorphization and dislocation generation mitigate the residual stresses developed on the interface. Consequently, anodes following DCR diffusion exhibit an ultrafast charging rate and alleviated self-limiting diffusion. Furthermore, dislocations generated near the propagating interface can act as a preferential pathway for diffusion because the activation energy for diffusion is lowered upon diffusion through dislocation cores. This accelerates the diffusion of carrier ions and facilitates the long-range diffusion of carrier ions at accelerated rates, which is typically known as “dislocation-pipe diffusion” [84, 87-89]. The transport rate of atoms during pipe diffusion is many orders of magnitude faster than that during bulk diffusion in a crystal [84, 90]. Therefore, in addition to the formation of a thin amorphous layer in front of the interface, dislocation-pipe diffusion in alloying anodes is an important mechanistic origin supporting the high rate performance of anode materials following DCR diffusion.

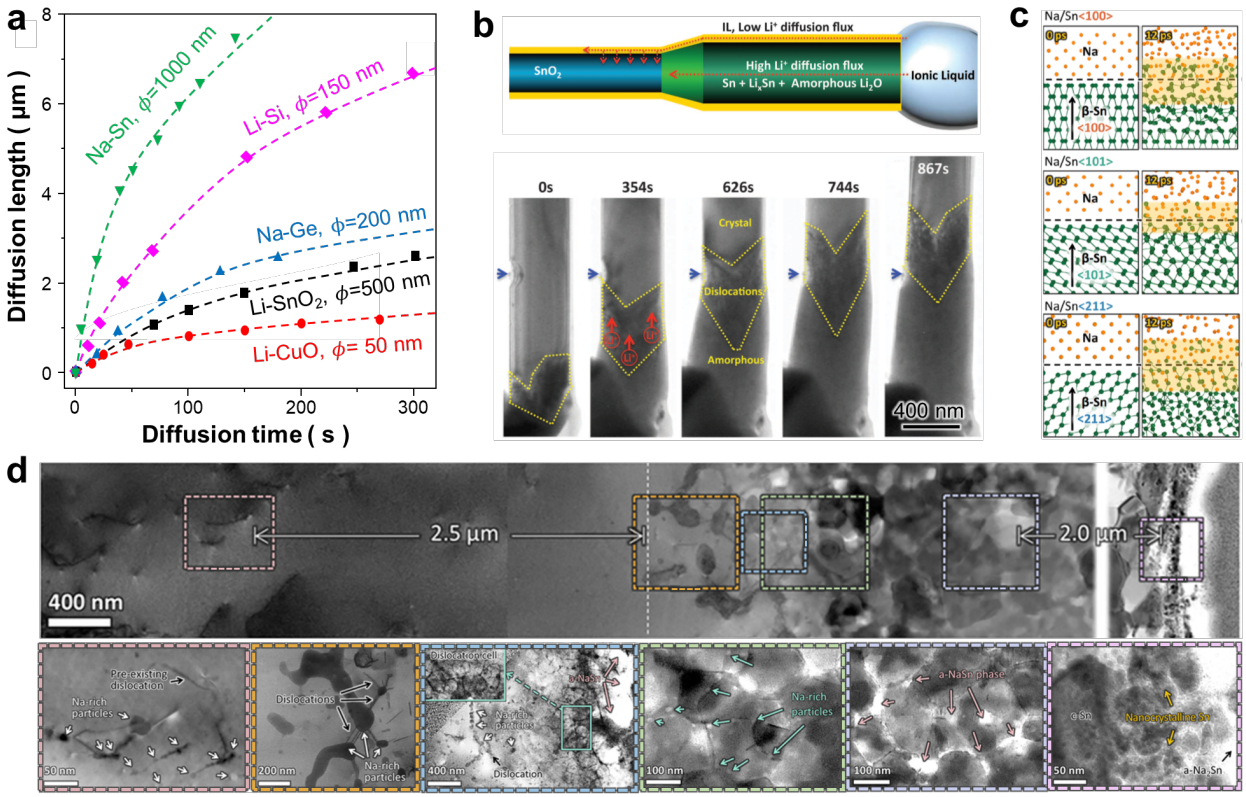

Figure 7. (a) *L* vs. *t* graphs constructed for various alloying anodes following DCR [19, 36, 46, 73, 82]. (b) Formation of dislocations in front of the propagating interface captured during lithiation of SnO_2 NWs, explaining the long-range diffusion of Li ions [36]. (c) DFT calculations showing the amorphization behavior of crystalline Sn near the interface [65]. (d) TEM images showing the formation of dislocations in crystalline Sn at regions away from the interface during sodiation [65].

455 **3.3. Carrier ion penetration depth and specific capacity**

456 Despite its large theoretical capacity, the alloying anode can only utilize limited capacity
457 during battery cycling (Figure 1). This low practical capacity is mainly attributed to the short
458 penetration depth of carrier ions into the anode material because the diffusion of carrier ions is
459 often arrested or self-limited inside the anode material, which hinders its full utilization. This
460 behavior, referred to as self-limiting diffusion (SLD), reveals itself as the limited practical capacity
461 of alloying anodes [77, 91]. Numerous efforts to understand the SLD behavior showed that it stems
462 from a large volumetric expansion and the development of residual stresses associated with the
463 diffusion of carrier ions [91, 92]. Therefore, the development of anodes with large energy capacity
464 relies on the ability to control the residual stresses developed in the alloying anodes.

465 Previous research on the diffusion behavior of alloying anodes reported that the residual
466 stresses developed in the anodes are closely related to the diffusion kinetics of carrier ions
467 (Sections 3.1 and 3.2). In this regard, diffusion kinetics can be a key concept for interpreting the
468 SLD behavior encountered in alloying anodes. In this section, we compare the SLD behavior of
469 alloying anodes governed by ICR and DCR diffusion kinetics and assess the relationship between
470 the diffusion kinetics and the practical capacity of alloying anodes.

471

472 **Systems governed by ICR:** Si, the most well-known alloying anode following ICR, is
473 known to exhibit SLD behavior with various solute atoms, including O [69], Li [77], and B [93]. For
474 the battery systems, SLD behavior occurring in the Li/Si couple began to gain attention in TEM
475 studies performed on the lithiation of Si NWs [94]. Experiments showed that lithiated Si NWs form
476 a core-shell structure consisting of unreacted Si at the interior and amorphous Li_xSi at the outer
477 layer. In the early 2010s, extensive TEM research was conducted to observe the SLD behavior of

Si NWs and Si NPs during lithiation. Liu et al. [77] observed the lithiation behavior of Si by directly attaching an Li_2O/Li electrode to a 129-nm-diameter Si NW and traced the movement of the reaction front (Figure 8a). The reaction front initially moved rapidly toward the interior of the Si NW, after which it gradually slowed down, before stopping completely after 1.5 hours of lithiation. This caused the lithiation of the Si NW to be arrested after penetrating only 55% of the entire volume of the Si NW. Model studies showed that the observed SLD phenomenon arises from the development of large compressive residual stresses at the sharp interface. Si NPs also suffer from the SLD behavior similar to that observed in Si NWs [50]; *in-situ* TEM studies showed that for all Si NPs with diameters of 90–200 nm, lithiation is impeded when the lithiated volume of Si NPs reaches approximately 50% (Figure 8b).

The SLD behavior of Si crystals can be explained by the increase in the Gibbs free energy (ΔG) estimated for the consumption of one Li ion to form $1/x$ units of Li_xSi:

$$\Delta G = \Delta G_r - e\phi + \frac{1}{x}[\bar{\sigma}_{Si}V_{Si} - \bar{\sigma}_{Li_xSi}V_{Li_xSi}], \qquad (1)$$

where ΔG_r is the free energy change in the absence of mechanical stress (σ) and applied voltage (ϕ). The second term ($-e\phi$) is the free energy decrease in the presence of the voltage applied to the electrochemical cell, whereas the third term in brackets is the increase in the free energy owing to the presence of mechanical stress in the structure, where $\bar{\sigma}_{Si}$ and $\bar{\sigma}_{Li_xSi}$ are the mean stress in the Si core at the interface and in the lithiated silicon, respectively, whereas V_{Si} and V_{Li_xSi} correspond to the volume of Si and Li_xSi, respectively. From an analysis of Eq. (1), the compressive stresses increase with increasing thickness of the lithiated layer, which suppresses further transportation of Li into Si NPs, and causes the SLD behavior. The SLD behavior was also observed in micrometer-scale Si structures [92] and other alloying anodes governed by ICR [44]. As discussed in the earlier Sections 3.1 and 3.2 and in detail in the following, high compressive

residual stresses are observed to develop in regions near the interface of the systems following ICR diffusion, suggesting that the SLD behavior can be attributed to this type of diffusion.

Although the above theories assisted in understanding of the relationship between the SLD behavior and ICR diffusion, these models cannot fully reproduce the SLD behavior of certain systems. For instance, the theories claimed that the SLD behavior of the Li/Si system occurs regardless of the initial size of Si NWs or NPs [50]. However, experimental studies on the lithiation of Si reported that, contrary to the model predictions, the penetration depth of carrier ions differs depending on the initial diameter of Si NPs. The full penetration of Li ions was observed for Si NPs with diameters smaller than 80 nm (Figure 8c) [71], whereas only partial lithiation for 140-nm-diameter Si NWs [43]. Subsequent studies interpreted this size-dependent SLD to arise, because the amount of stress-induced energy (σV) accumulated near the interface was relatively small for Si NWs with small diameters [71]. In addition to the above examples, the full lithiation of Si was also observed in Si NPs with an amorphous structure (Figure 8d). The amorphous Si phase can readily relieve the compressive residual stresses developed at the interface via structural relaxation, which allows the lithiation to proceeds toward the Si core. The above examples demonstrating the full lithiation of Si indicate that the numerical models based on the continuum theory alone are insufficient to fully interpret the SLD behaviors. This is because, when viewed at the atomic scale, the SLD behavior is closely related to the structural changes, such as amorphization [44, 65] and dislocation generation [36, 65], which can partially relieve residual stresses. This will be explained in detail in the following by relating the structural changes to the DCR diffusion.

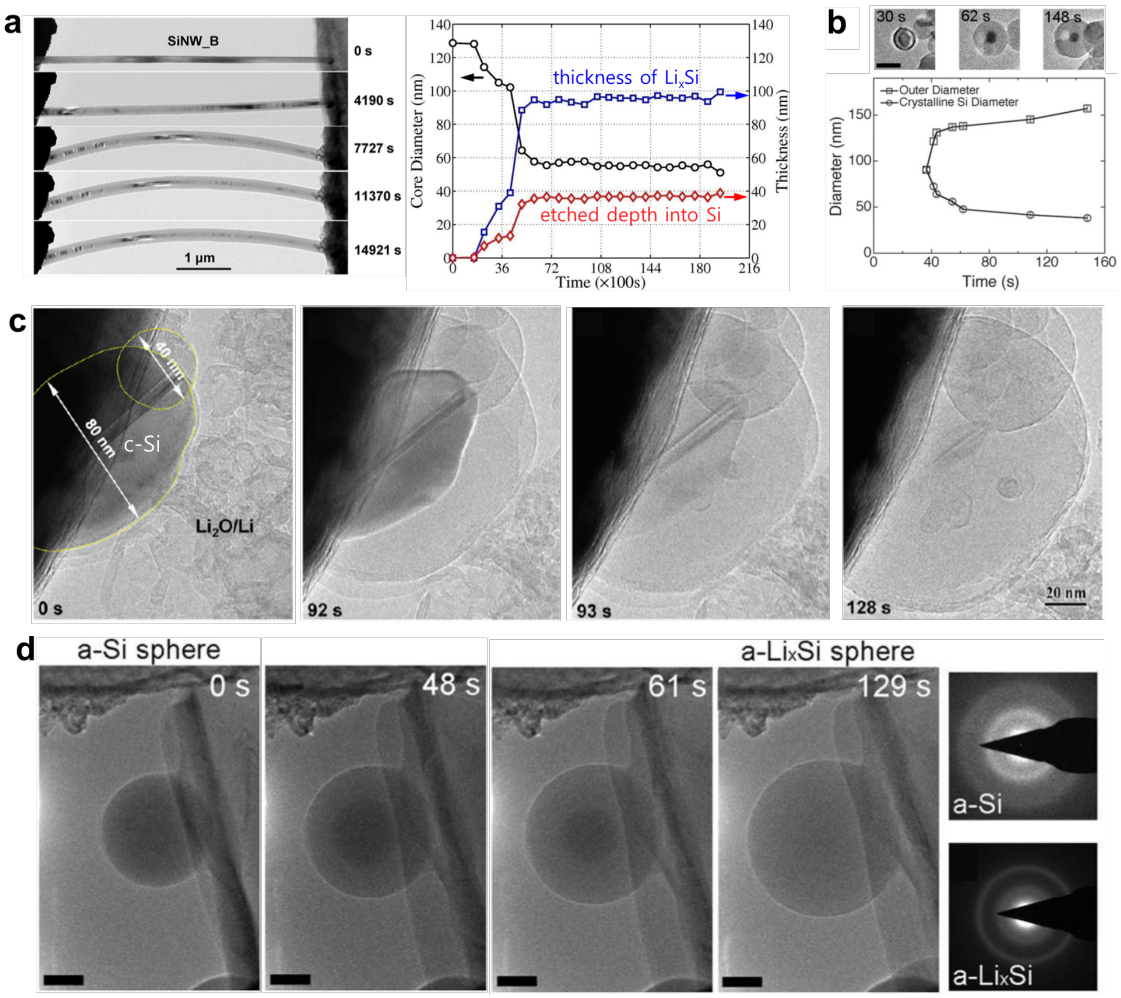

Figure 8. Self-limiting lithiation behavior observed in: (a) 129-nm-diameter Si NW [77] and (b) 90-nm-diameter Si NPs [50]. TEM images showing the full lithiation of Si NPs captured during lithiation of: (c) crystalline Si NPs [71], and (d) amorphous Si NPs [75].

Systems governed by DCR: Of various anodes following DCR, Ge is the first material for which the penetration behavior of carrier ions was observed. Lithiation experiments performed on Ge showed that, while having the same crystal structure as Si, the SLD behavior is significantly mitigated for Ge. When a 165-nm-diameter Ge NW was in contact with Li, Li ions penetrated into the core of the Ge NW, transforming Ge into $Li_{15}Ge_4$ (Figure 9a) [95]. In another experiment, the

full lithiation in Ge NPs with various diameters of 160–620 nm was observed (Figure 9b) [96]. The lithiation behavior of Ge crystals largely differ from those observed in Si crystals that display SLD even for 130-nm-diameter Si NWs (Figure 8a). This suggests that the threshold diameter for SLD is larger for Ge than for Si, indicating that the anode materials following DCR diffusion can fully utilize their theoretical capacity even for a relatively large size. Furthermore, close examination of lithiated Ge revealed additional features, e.g., compared to the sharp and straight interface and anisotropic expansion observed in the Li/Si system, the Li/Ge system displays an obscure and tortuous interface and expands isotropically. This indicates that the atomic scale interactions occurring at the Ge/Li_xGe interface differ from those at the Si/Li_xSi interface.

To better understand the physics behind the SLD behavior, Park et al. [44] performed a comparative study on the Na/Sb and Na/Sn systems governed by ICR and DCR, respectively. They observed the structural evolution near the interface of the two systems and established a relationship between the diffusion kinetics and SLD behavior. Compared to the Na/Sb system (ICR), the Na/Sn system (DCR) exhibits a much deeper penetration of Na into Sn, while forming a tortuous and obscure Sn/Na_xSn interface (Figure 9c). Subsequent DFT calculations showed that in the Na/Sb system, Na ions diffuse toward crystalline Sb, while the initial crystal structure of Sb is retained. This not only requires high energy for diffusion, but also leads to the development of residual stresses near the interface, which arrests Na diffusion into Sb. Conversely, Na diffusion in the Na/Sn system proceeds by forming a thin amorphous layer in front of the advancing interface [65]. The amorphization alleviates the residual stress development near the interface, which, in turn, permits the additional penetration of Na ions into the Sn interior.

Another important structural evolution affecting the SLD behavior is the generation of dislocations preceding an advancing interface. TEM observations near the interface of the Na/Sn

system showed that residual stresses developed in regions near the propagating interface can generate dislocations near the interface [65]. Thus-formed dislocations in a Sn crystal not only relieve the stress-induced energy, but also promote the transport of Na ions through dislocation cores, by attracting Na ions into their open spaces. Continual supply of Na atoms via this dislocation-pipe diffusion causes Na-rich particles to grow, which results in a localized plastic yielding of the adjacent crystalline Sn grains by generating a dislocation burst. The repetition of the pipe diffusion and generation of additional dislocations increase significantly the penetration depth of Na ions, which mitigates the SLD behavior and improves the practical capacity of Sn anodes.

The relationship between the SLD behavior and diffusion kinetics can further be explained by relating the various experimental observations to the measured residual stresses near the interfaces [97]. For the Li/Si system governed by ICR diffusion, lithiated Si develops a large misfit strains and the associated compressive residual stresses near the Si/Li_xSi interface (Figure 9d). The compressive stresses increase the stress-induced energy term (σV) in Eq. (1), which in turn increases the overall driving force of Li diffusion and causes the SLD behavior. Conversely, for systems governed by DCR, the diffusion of carrier ions is often accompanied by the disruption of crystalline structures and generation of dislocations, which can reduce the stress-induced energy term and thus increase the driving force of diffusion. This was confirmed by stress measurements at the atomic scale performed on a partially sodiated Sn anode, where the residual stresses develop near the Sn/Na_xSn interface were much smaller than those measured at the Si/Li_xSi interface (Figure 9e). Such low residual stresses cause Na ions to diffuse much deeper into Sn anode at fast rates, which allows Sn anodes to fully utilize their theoretical capacity.

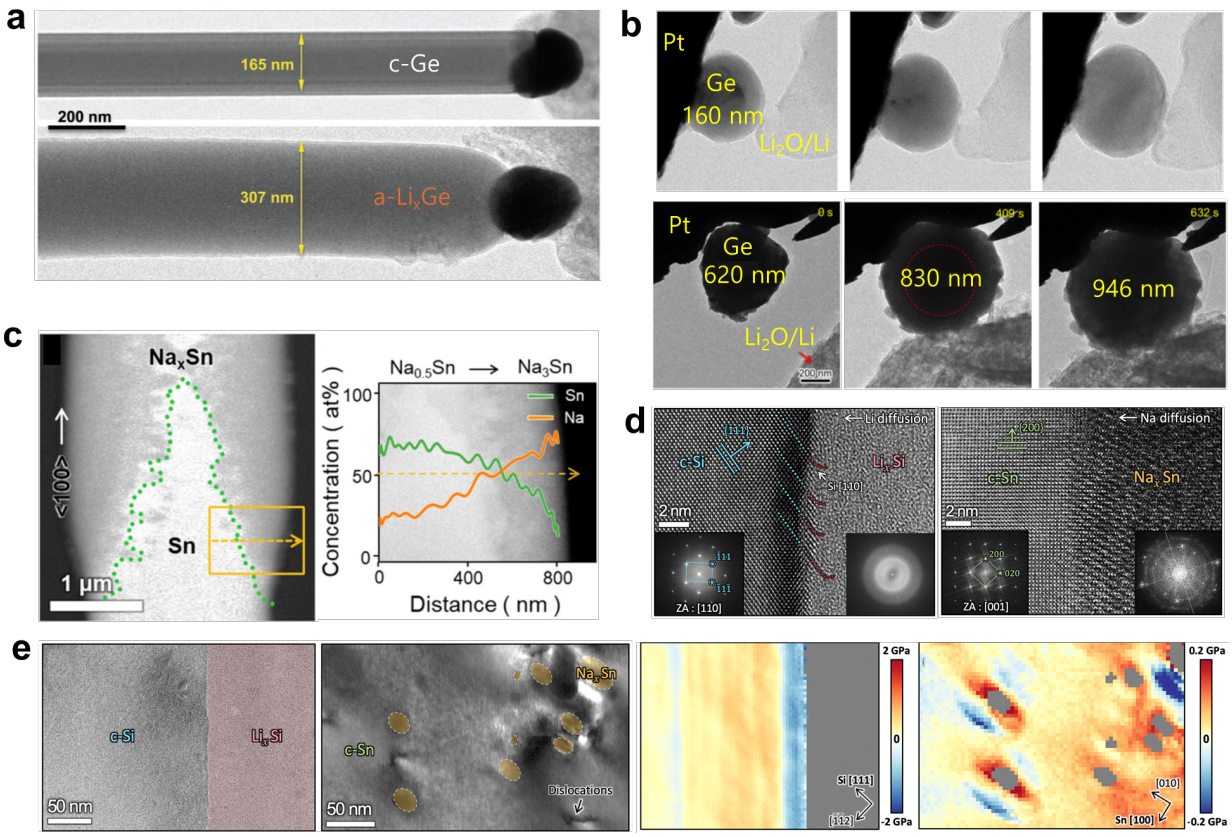

Figure 9. TEM images captured during *in-situ* lithiation experiments performed on: (a) a 165-nm-diameter Ge NW [95], and (b) 160- and 620-nm-diameter Ge NPs [96]. (c) Back-scattered electron image and energy-dispersive X-ray spectroscopy line profiles recorded from longitudinal cross-section near propagating phase boundary of sodiated Sn pillar [44]. (d) High-resolution TEM images of interfacial structure recorded at Si/Li_xSi and Sn/Na_xSn interfaces in Li/Si and Na/Sn systems, respectively [97]. (e) Comparison of interfacial microstructures and corresponding residual stress distributions near interface of Li/Si and Na/Sn systems [97].

4. Summary and Outlook

In this brief progress report, we summarize the research history of diffusion kinetics and how this concept can be used to interpret the origin of the electrochemical performances of alloying anodes. The previous theories on diffusion kinetics developed generic criteria of DCR and ICR

diffusion, which is revealed in experiments by the parabolic ($L^2 \propto t$) and linear ($L \propto t$) rate laws, respectively. Experimental and theoretical studies that aimed to develop high-performance alloying anodes highlighted the importance of diffusion kinetics on the cycle life, rate performance, and practical capacity of anodes. Overall, alloying anodes (e.g., Si, Sb, and P) following ICR commonly show diffusion behaviors, such as anisotropic volume changes, slow diffusion rate, and self-limiting diffusion, which can deteriorate the anode performance during battery cycling. The mechanistic origin of the diffusion kinetics governed by ICR is ascribed to the diffusion of carrier ions by forming a sharp two-phase boundary and abrupt compositional changes across the interface, which develops large residual compressive stresses and impedes further diffusion of carrier ions.

Contrary to ICR-governed alloying anodes, those following DCR commonly show isotropic volume changes, a comparatively fast diffusion rate, and reduced self-limiting diffusion, which can improve the anode performance during battery cycling. The criteria to select DCR-governed alloying anodes are based on the interatomic bond strength and yield strength of alloying-anode materials, which can be used as the indicators to assess the ease of diffusion at the interface. When carrier ions diffuse into a low-yielding anode material with a weak interatomic bond strength, carrier-ion diffusion often proceeds by the formation of an amorphous layer and dislocations at the unreacted anode material close to the advancing interface [51]. These structural changes can readily relieve residual stresses at the propagating interface and thus facilitate the rapid inflow of carrier ions into the unreacted anode following DCR diffusion. The diffusion behaviors displayed by DCR-governed anodes can also be beneficial in practical applications, of which examples are discussed in the following.

Reducing the fabrication cost of long-lasting alloying anodes: With regard to the issues

related to relieving residual stresses and improving the cyclability of anodes, some achievements have been made with the design of nanostructure and composite anodes. In light of the size-dependent residual stresses developed in alloying anodes, the use of nanostructured anodes has become a common means by which to prevent anode degradation and improve the cycle life. Nanoscale materials, owing to their large surface-to-volume ratio, can reduce the development of residual stresses [98], which, in turn, can mitigate the reduction of the electrochemical performance arising from ICR diffusion. In addition to nanoscale structures, porous structures can also alleviate the residual stresses caused by large volume changes associated with battery cycling [99-101]. Recently, coating and doping of Si and Ge anodes with other elements have also been considered to be effective in controlling volume expansions and associated residual stresses [43, 81].

Although the above synthesis strategies have greatly improved the cyclability of alloying anodes, there remain critical issues regarding their production costs and complexity. In this respect, the selection of anode materials governed by DCR can provide better battery performance while reducing the additional fabrication cost; when Si and Ge NWs that follow the different diffusion kinetics of ICR and DCR, respectively, are compared, the threshold diameter for the fracture of NWs during lithiation is much larger for Ge (1200 nm) [72] than that for Si (300 nm) [71]. Furthermore, the critical diameter for full lithiation is also larger for Ge NPs (~620 nm) [96] than for Si NPs (~130 nm) [77]. These large threshold diameters of Ge allow it to exhibit high mechanical stability and large practical capacity even for anodes with a large size, which requires less fabrication cost than the Si counterparts [95]. This suggests that, although the use of nanostructured anodes is effective in improving the cyclability of anodes, the choice of anode materials following DCR diffusion could be another alternative for enhancing the same property.

Improving the rate performance of the conversion–alloying anodes: In addition to the Group IVA and VA elements (e.g., Si, Ge, and Sn) discussed in this review, metal oxide anodes (M_xO_y, M = Zn, Sn, Sb, etc.) also undergo alloying reactions during battery cycling and have emerged as another important class of anodes for future applications. Some representative examples include ZnO and SnO_2 for Li-ion batteries [102] and SnO_x and Sb_2O_3 for Na-ion batteries [17]. The charging and discharging processes of these anodes proceed by following the mechanism known as the "conversion–alloying reaction"; the initial irreversible conversion reaction occurs between M_xO_y and the charge carriers (Li or Na), and this is followed by the reversible alloying reaction occurring between the reduced M and the charge carriers, according to Eqs. (2) and (3), respectively.

$$M_xO_y + 2yLi^+ + 2ye^- \rightarrow xM + yLi_2O \qquad (2)$$

$$xM + zLi^+ + ze^- \leftrightarrow Li_zM_x \qquad (3)$$

In addition to metal oxides, metal sulfides (SnS_2, Sb_2S_3) also follow the conversion–alloying mechanism [17, 102].

The excellent electrochemical performances of conversion–alloying anodes are attributed to the formation of the Li_2O (or Na_2O) phase in Eq. (2). The major advantage of Li_2O is that it can mechanically buffer the volumetric expansion during battery cycling and thus improve the cycle life of anodes [102]. This is particularly true during the subsequent alloying reaction in Eq. (3). Although the reaction given by Eq. (3) normally causes the volume of the anode to expand by greater than 300% [48, 49], the development of residual stresses in the anodes can be reduced by the presence of the buffer Li_2O phase, which reduces the energy barrier for diffusion and retards the crack formation and pulverization of the anode materials. Another important feature of the Li_2O phase is its electrochemical inactivity during battery cycling. According to previous studies on

660 typical conversion anodes of TMO_x (TM = transition metal), the reduction or oxidation of Li_2O
661 during battery cycling requires a large amount of energy, which is revealed in voltametric
662 experiments as a large hysteresis loss and thus low energy efficiency of the anodes [103, 104].
663 However, unlike the Li_2O formed in conversion anodes, the same phase formed in conversion–
664 alloying anodes does not react with inflowing/outflowing Li ions, rendering the anode to manifest
665 low-voltage hysteresis and thus high energy efficiency. However, despite the advantages
666 associated with the formation of Li_2O in conversion–alloying anodes, its poor electric conductivity
667 impedes the diffusion of carrier ions and, in turn, limits the rate performance of the anodes. To
668 solve this problem, research on conversion–alloying anodes hybridized with electrically
669 conductive carbon/graphite is currently underway [105, 106].

670 Together with the incorporation of carbonaceous materials, the use of anode materials
671 governed by DCR diffusion can further improve the rate performance of conversion–alloying
672 anodes. As can be seen from the conversion–alloying reactions in Eqs. (2) and (3), the initial
673 conversion reaction is irreversible, whereas the subsequent alloying reaction is reversible during
674 repeated battery cycles. This indicates that the electrochemical performance of these anodes is
675 primarily determined by the alloying reaction, not by the conversion reaction. From this
676 perspective, the concept of the diffusion kinetics of alloying anodes discussed earlier can also be
677 extended to the conversion–alloying anodes. Because alloying anodes following DCR diffusion
678 exhibit faster penetration of the charge carriers into the anodes, conversion–alloying anodes mixed
679 with alloying anodes could display an improved rate performance by taking the advantages of
680 DCR diffusion. There is an increasing number of evidential reports that support this hypothetical
681 concept. Representative examples are SnO_2 [107] and Bi_2O_3 [108], both of which exhibit long
682 cyclability under fast charging/discharging rates.

683

684 **Developing anodes for high-power applications:** The two main techniques used to
685 understand the carrier-ion diffusion under high-power operations are the (1) galvanostatic and (2)
686 potentiostatic modes of diffusion experiments. The diffusion of carrier ions under the galvanostatic
687 and potentiostatic modes are controlled by the current density and the electric field (or potential)
688 in the anodes, respectively. From an atomistic perspective, the former operation uses a constant
689 flux of carrier ions in the anode, whereas the latter maintains the constant concentration of the
690 carrier ions at the anode's surface [109]. Although the two methods appear to be different from each
691 other, both methods have the same effect in enhancing the diffusion rate of the carrier ions; the
692 greater the current density (or electric field) applied in the anodes, the faster and deeper the carrier
693 ions diffuse into the anodes. This behavior was well observed from the lithiation of Si measured
694 as a function of the current density [92]. Experiments have shown that the penetration depths of Li
695 diffusion into Si increase with increasing current density, while maintaining the preferential
696 diffusion direction along <110> of crystalline Si. This indicates that the practical capacity of the
697 alloying anodes can be increased simply by increasing the current density or the electric field.

698 Although increasing the electric field or the current density is beneficial for improving the
699 capacity of anodes, both methods are ultimately limited by the Li (or Na) diffusivity of the
700 electrode materials. When the current rate of the anodes exceeds the threshold current rate (also
701 referred to as the "diffusion-limited C-rate"), the diffusional flux of carrier ions in the anodes is
702 no longer able to keep up with the current rate, resulting in the depletion of carrier ions in the
703 cathodes (anodes) during discharging (charging) [110]. This depletion in the charge carriers causes
704 a substantial decrease in the capacity of the battery [111]. This phenomenon occurs because the
705 diffusivity of the carrier ions in the electrodes is slower than the current rate applied during high-

power operations.

The concept of the diffusion kinetics of alloying anodes discussed in this review can be used to develop high-power-density batteries. Owing to their ability to form an amorphous layer and high-density dislocations near the propagating interface (see Figures 7c–d), alloying anodes following DCR diffusion enable the faster diffusion of carrier ions into the anodes. When the diffusivities of alloying anodes are compared, the diffusivities (~3.0×10^{-6} cm^2 s^{-1} for Na–Sn [82] and ~3.6×10^{-7} cm^2 s^{-1} for Na–Ge [112]) of carrier ions in DCR-governed alloying anodes are greater than those (~5.1×10^{-12} cm^2 s^{-1} for Li–Si [113] and ~3.0×10^{-10} cm^2 s^{-1} for Na–Sb [114]) of ICR-governed alloying anodes by more than three to five orders of magnitude. Therefore, the selection of the DCR-governed alloying anodes can prevent the depletion of charge carriers at high current rates, making them suitable for the high-power operations. In addition to the works on improving ionic diffusivity in anodes, additional studies have reported the electric resistivity associated with the occurrence of phase transition during battery cycling is also important in developing anodes for high-power applications [115-117]. Further experimental and theoretical studies on the effect of the current rate on diffusion behaviors are required to realize alloying anodes suitable for high-power operations.

Although the present review has mainly focused on the diffusion kinetics of alloying anodes, the diffusion behaviors in practical batteries are more complicated and are determined by various external factors. In particular, the electrolyte conditions and associated solid-electrolyte interfaces (SEIs) formed during battery cycles can play an important role in determining the diffusion behaviors of carrier ions. This is especially true when the diffusivity of the carrier ions is lower in the SEIs than in the anodes [118, 119]. For instance, the carrier-ion diffusivity (~1.8×10^{-13} to

729 7.6×10^{-11} cm^2 s^{-1} [120]) in SEIs is much lower than the typical values (e.g., ~3.0×10^{-6} cm^2 s^{-1}
730 for Na–Sn [82] and ~3.6×10^{-7} cm^2 s^{-1} for Na–Ge [112]) in DCR-governed alloying anodes. In this
731 case, the overall diffusion rate is limited by the SEI, rather than by the propagating interface or the
732 trailing bulk region. Furthermore, the large volumetric expansion of the alloying anodes during
733 lithiation/sodiation can readily destroy the SEI layer formed on the anode surface. All of these
734 behaviors, although lowering the rate performance of the anodes, can alter the diffusion kinetics
735 and associated diffusion behaviors (e.g., anisotropic/isotropic swelling and penetration depth) of
736 the anodes. Therefore, to realize batteries for practical applications, it is essential to optimize the
737 electrolyte conditions and the associated SEIs.

738 Various technical approaches have been devoted to minimizing the detrimental effects of the
739 SEIs on the alloying anodes. The addition of electrolyte additives [121, 122] and the coating of the
740 anode with conductive artificial SEIs [123-125] are the effective ways to improve the diffusivity of
741 carrier ions in the SEIs. Other strategies include the enhancement of the structural stability of SEIs
742 dissolving appropriate salts [126] or additives [127, 128] in the electrolyte solution and the coating of
743 the anode surface with a conductive and stable carbon layer [129]. Although discussions on the
744 electrolyte conditions and SEIs were not covered in detail in this review, the strategies to optimize
745 the electrolyte conditions, in combination with the diffusion kinetics of the alloying anodes, are
746 the key to developing the anodes for future batteries.

747

748 **Acknowledgements**

749 This work was supported by the National Research Foundation of Korea (NRF) grant funded by
750 the Korea government (MEST, NRF-2018R1A2B6003927). YSC and DOS are indebted to the
751 Faraday Institution NEXGENNA project (FIRG018) for financial support.

Corresponding Author

E-mail: jclee001@korea.ac.kr (JCL).

ORCID

Yong-Seok Choi: 0000-0002-3737-2989

David O. Scanlon: 0000-0001-9174-8601

Jae-Chul Lee: 0000-0002-9294-2163

Notes

The authors declare no competing financial interest.

Biographies

Yong-Seok Choi is a postdoctoral researcher at the Department of Chemistry, University College London. He received his Ph.D. from the Department of Materials Science and Engineering at Korea University in February 2020. He specializes in the application of first-principles techniques for elucidating electronic/atomic structures governing the electrochemical performance of energy storage materials. His experience and interests include electrodes and solid electrolytes for Na-ion batteries.

Jae-Chul Lee is a full professor at the College of Engineering, Korea University. He received his B.S. from Korea University, South Korea, in 1985, and his M.S. and Ph.D. in materials science from Michigan State University in 1989 and 1992, respectively. His recent research interests include atomic simulations for elucidating the electric/chemical/mechanical properties of structural materials and batteries.

David O. Scanlon is the Chair of Computational Materials Design at the Department of Chemistry at University College London and at Diamond Light Source. He received his B. A. (Mod) in Computational Chemistry and PhD in Chemistry from Trinity College Dublin, Ireland in 2006 and 2011 respectively. His work is at the forefront of the global effort to explore new materials based on computations and to advance the capacity of first-principles calculations to predict materials properties.

References

[1] J.-M. Tarascon, M. Armand, in *Materials for sustainable energy: a collection of peer-reviewed research and review articles from Nature Publishing Group*, World Scientific, Republic of Singapore 2011, 171.

[2] N. Nitta, F. Wu, J. T. Lee, G. Yushin, *Mater. Today* **2015**, *18*, 252.

[3] P. K. Nayak, E. M. Erickson, F. Schipper, T. R. Penki, N. Munichandraiah, P. Adelhelm, H. Sclar, F. Amalraj, B. Markovsky, D. Aurbach, *Adv. Energy Mater.* **2018**, *8*, 1702397.

[4] C. Capasso, O. Veneri, *Appl. Energy* **2014**, *136*, 921.

[5] P. Gibot, M. Casas-Cabanas, L. Laffont, S. Levasseur, P. Carlach, S. Hamelet, J.-M. Tarascon, C. Masquelier, *Nat. Mater.* **2008**, *7*, 741.

[6] M. Noel, V. Suryanarayanan, *J. Power Sources* **2002**, *111*, 193.

[7] J. Xu, F. Lin, M. M. Doeff, W. Tong, *J. Mater. Chem. A* **2017**, *5*, 874.

[8] P. Rozier, J. M. Tarascon, *J. Electrochem. Soc.* **2015**, *162*, A2490.

[9] L. Zhang, M. A. Reddy, X.-M. Lin, Z. Zhao-Karger, M. Fichtner, *J. Alloys Compd.* **2017**, *724*, 1101.

[10] Y. Lu, L. Yu, X. W. D. Lou, *Chem* **2018**, *4*, 972.

[11] H. Yin, Q. Li, M. Cao, W. Zhang, H. Zhao, C. Li, K. Huo, M. Zhu, *Nano Res.* **2017**, *10*, 2156.

[12] A. M. Chockla, K. C. Klavetter, C. B. Mullins, B. A. Korgel, *ACS Appl. Mater. Inter.* **2012**, *4*, 4658.

[13] J. Qian, D. Qiao, X. Ai, Y. Cao, H. Yang, *Chem. Commun.* **2012**, *48*, 8931.

[14] C.-M. Park, S. Yoon, S.-I. Lee, J.-H. Kim, J.-H. Jung, H.-J. Sohn, *J. Electrochem. Soc.* **2007**, *154*, A917.

[15] Y. Yao, M. T. McDowell, I. Ryu, H. Wu, N. Liu, L. Hu, W. D. Nix, Y. Cui, *Nano Lett*. **2011**, *11*, 2949.

[16] W. M. Zhang, J. S. Hu, Y. G. Guo, S. F. Zheng, L. S. Zhong, W. G. Song, L. J. Wan, *Adv. Mater*. **2008**, *20*, 1160.

[17] H. Zhang, I. Hasa, S. Passerini, *Adv. Energy Mater*. **2018**, *8*, 1702582.

[18] M. J. Chon, V. A. Sethuraman, A. McCormick, V. Srinivasan, P. R. Guduru, *Phys. Rev. Lett*. **2011**, *107*, 045503.

[19] X. H. Liu, H. Zheng, L. Zhong, S. Huang, K. Karki, L. Q. Zhang, Y. Liu, A. Kushima, W. T. Liang, J. W. Wang, *Nano Lett*. **2011**, *11*, 3312.

[20] Z. Cui, F. Gao, J. Qu, *J. Mech. Phys. Solids* **2013**, *61*, 293.

[21] H. Schmalzried, *Chemical kinetics of solids*, John Wiley & Sons, Germany **2008**.

[22] D. J. Young, *High temperature oxidation and corrosion of metals*, Vol. 1, Elsevier, Netherlands **2008**.

[23] H. Schmalzried, *Solid-State Reactions between Oxides* in *Defects and transport in oxides*, Springer, Germany **1974**, 83.

[24] M. H. Davies, C. E. Birchenall, *JOM* **1951**, *3*, 877.

[25] V. B. Voitovich, V. A. Lavrenko, V. M. Adejev, E. I. Golovko, *Oxid. Met*. **1995**, *43*, 509.

[26] H. I. Aaronson, T. Abe, J. Bradley, W. A. Clark, T. Obara, *Mater. Sci*. **1979**.

[27] P. W. Bach, *Vol. 13*, *Technische Hogeschool Twente* **1981**, 1.

[28] R. M. Cannon, W. H. Rhodes, A. H. Heuer, *J. Am. Ceram. Soc*. **1980**, *63*, 46.

[29] P. Murray, G. F. Carey, *J. Comput. Phys*. **1988**, *74*, 440.

[30] P. Murray, G. F. Carey, *J. Appl. Phys*. **1989**, *65*, 3667.

[31] G. P. Krielaart, J. Sietsma, S. Van Der Zwaag, *Mater. Sci. Eng. A* **1997**, *237*, 216.

[32] C. R. Gorla, W. E. Mayo, S. Liang, Y. Lu, *J. Appl. Phys.* **2000**, *87*, 3736.

[33] C. Korte, N. Ravishankar, C. B. Carter, H. Schmalzried, *Solid State Ion.* **2002**, *148*, 111.

[34] J. K. Farrer, C. B. Carter, *J. Mater. Sci.* **2006**, *41*, 5169.

[35] T. Akashi, M. Nanko, T. Maruyama, Y. Shiraishi, J. Tanabe, *J. Electrochem. Soc.* **1998**, *145*, 2090.

[36] J. Y. Huang, L. Zhong, C. M. Wang, J. P. Sullivan, W. Xu, L. Q. Zhang, S. X. Mao, N. S. Hudak, X. H. Liu, A. Subramanian, *Science* **2010**, *330*, 1515.

[37] S. W. Lee, M. T. McDowell, J. W. Choi, Y. Cui, *Nano Lett.* **2011**, *11*, 3034.

[38] A. F. Bower, P. R. Guduru, V. A. Sethuraman, *J. Mech. Phys. Solids* **2011**, *59*, 804.

[39] Z. Cui, F. Gao, J. Qu, *J. Mech. Phys. Solids* **2012**, *60*, 1280.

[40] K. Zhao, M. Pharr, Q. Wan, W. L. Wang, E. Kaxiras, J. J. Vlassak, Z. Suo, *J. Electrochem. Soc.* **2011**, *159*, A238.

[41] J.-H. Seo, C.-Y. Chou, Y.-H. Tsai, Y. Cho, T.-Y. Seong, W.-J. Lee, M.-H. Cho, J.-P. Ahn, G. S. Hwang, I.-S. Choi, *RSC Adv.* **2015**, *5*, 17438.

[42] X. H. Liu, J. W. Wang, S. Huang, F. Fan, X. Huang, Y. Liu, S. Krylyuk, J. Yoo, S. A. Dayeh, A. V. Davydov, *Nat. Nanotech.* **2012**, *7*, 749.

[43] X. H. Liu, L. Q. Zhang, L. Zhong, Y. Liu, H. Zheng, J. W. Wang, J.-H. Cho, S. A. Dayeh, S. T. Picraux, J. P. Sullivan, *Nano Lett.* **2011**, *11*, 2251.

[44] J.-H. Park, Y.-S. Choi, Y.-W. Byeon, J.-P. Ahn, J.-C. Lee, *Nano Energy* **2019**, *65*, 104041.

[45] X. H. Liu, S. Huang, S. T. Picraux, J. Li, T. Zhu, J. Y. Huang, *Nano Lett.* **2011**, *11*, 3991.

[46] X. Lu, E. R. Adkins, Y. He, L. Zhong, L. Luo, S. X. Mao, C.-M. Wang, B. A. Korgel, *Chem. Mater.* **2016**, *28*, 1236.

[47] E. W. Haycock, *J. Electrochem. Soc.* **1959**, *106*, 771.

[48] J. Woods, N. Bhattarai, P. Chapagain, Y. Yang, S. Neupane, *Nano Energy* **2019**, *56*, 619.

[49] M. Lao, Y. Zhang, W. Luo, Q. Yan, W. Sun, S. X. Dou, *Adv. Mater.* **2017**, *29*, 1700622.

[50] M. T. McDowell, I. Ryu, S. W. Lee, C. Wang, W. D. Nix, Y. Cui, *Adv. Mater.* **2012**, *24*, 6034.

[51] Y.-S. Choi, J.-H. Park, J.-P. Ahn, J.-C. Lee, *Chem. Mater.* **2019**, *31*, 1696.

[52] H. Mehrer, *Diffusion in solids: fundamentals, methods, materials, diffusion-controlled processes*, Vol. 155, Springer Science & Business Media, United States **2007**.

[53] H. Yang, S. Huang, X. Huang, F. Fan, W. Liang, X. H. Liu, L.-Q. Chen, J. Y. Huang, J. Li, T. Zhu, *Nano Lett.* **2012**, *12*, 1953.

[54] H. Jung, M. Lee, B. C. Yeo, K.-R. Lee, S. S. Han, *J. Phys. Chem. C* **2015**, *119*, 3447.

[55] A. Ostadhossein, E. D. Cubuk, G. A. Tritsaris, E. Kaxiras, S. Zhang, A. C. T. Van Duin, *Phys. Chem. Chem. Phys.* **2015**, *17*, 3832.

[56] J. Rohrer, A. Moradabadi, K. Albe, P. Kaghazchi, *J. Power Sources* **2015**, *293*, 221.

[57] M. K. Y. Chan, C. Wolverton, J. P. Greeley, *J. Am. Chem. Soc.* **2012**, *134*, 14362.

[58] H. Tachikawa, Y. Nagoya, T. Fukuzumi, *J. Power Sources* **2010**, *195*, 6148.

[59] H. Tachikawa, *J. Phys. Chem. C* **2007**, *111*, 13087.

[60] H. Tachikawa, A. Shimizu, *J. Phys. Chem. B* **2005**, *109*, 13255.

[61] Y.-S. Choi, J.-H. Park, J.-P. Ahn, J.-C. Lee, *Sci. Rep.* **2017**, *7*, 1.

[62] W. Xia, Q. Zhang, F. Xu, H. Ma, J. Chen, K. Qasim, B. Ge, C. Zhu, L. Sun, *J. Phys. Chem. C* **2016**, *120*, 5861.

[63] J. Sun, H.-W. Lee, M. Pasta, H. Yuan, G. Zheng, Y. Sun, Y. Li, Y. Cui, *Nat. Nanotech.* **2015**, *10*, 980.

[64] T. Chen, P. Zhao, X. Guo, S. Zhang, *Nano Lett.* **2017**, *17*, 2299.

[65] Y.-W. Byeon, Y.-S. Choi, J.-P. Ahn, J.-C. Lee, *ACS Appl. Mater. Inter.* **2018**, *10*, 41389.

[66] B. Schwartz, *J. Electrochem. Soc.* **1967**, *114*, 285.

[67] R. Leancu, N. Moldovan, L. Csepregi, W. Lang, *Sens. Actuators A* **1995**, *46*, 35.

[68] Y.-S. Choi, Y.-W. Byeon, J.-P. Ahn, J.-C. Lee, *Nano Lett.* **2017**, *17*, 679.

[69] B.-H. Kim, M. Ariesto Pamungkas, M. Park, G. Kim, K.-R. Lee, Y.-C. Chung, *Appl. Phys. Lett.* **2011**, *99*, 143115.

[70] T. Kennedy, M. Brandon, K. M. Ryan, *Adv. Mater.* **2016**, *28*, 5696.

[71] I. Ryu, J. W. Choi, Y. Cui, W. D. Nix, *J. Mech. Phys. Solids* **2011**, *59*, 1717.

[72] S. W. Lee, I. Ryu, W. D. Nix, Y. Cui, *Extreme Mech. Lett.* **2015**, *2*, 15.

[73] M. Sun, K. Qi, X. Li, Q. Huang, J. Wei, Z. Xu, W. Wang, X. Bai, *ChemElectroChem* **2016**, *3*, 1296.

[74] M. T. McDowell, S. W. Lee, I. Ryu, H. Wu, W. D. Nix, J. W. Choi, Y. Cui, *Nano Lett.* **2011**, *11*, 4018.

[75] M. T. McDowell, S. W. Lee, J. T. Harris, B. A. Korgel, C. Wang, W. D. Nix, Y. Cui, *Nano Lett.* **2013**, *13*, 758.

[76] J. W. Wang, Y. He, F. Fan, X. H. Liu, S. Xia, Y. Liu, C. T. Harris, H. Li, J. Y. Huang, S. X. Mao, *Nano Lett.* **2013**, *13*, 709.

[77] X. H. Liu, F. Fan, H. Yang, S. Zhang, J. Y. Huang, T. Zhu, *ACS Nano* **2013**, *7*, 1495.

[78] A. D. Drozdov, P. Sommer-Larsen, J. deClaville Christiansen, *J. Appl. Phys.* **2013**, *114*, 223514.

[79] T. Shimura, M. Shimizu, S. Horiuchi, H. Watanabe, K. Yasutake, M. Umeno, *Appl. Phys. Lett.* **2006**, *89*, 111923.

[80] K.-W. Park, C.-M. Lee, M. Wakeda, Y. Shibutani, M. L. Falk, J.-C. Lee, *Acta Mater*. **2008**, *56*, 5440.

[81] L. C. Loaiza, L. Monconduit, V. Seznec, *Small* **2020**, *16*, 1905260.

[82] Y.-S. Choi, Y.-W. Byeon, J.-H. Park, J.-H. Seo, J.-P. Ahn, J.-C. Lee, *ACS Appl. Mater. Inter*. **2018**, *10*, 560.

[83] A. Nie, L.-Y. Gan, Y. Cheng, H. Asayesh-Ardakani, Q. Li, C. Dong, R. Tao, F. Mashayek, H.-T. Wang, U. Schwingenschlögl, *ACS Nano* **2013**, *7*, 6203.

[84] M. Legros, G. Dehm, E. Arzt, T. J. Balk, *Science* **2008**, *319*, 1646.

[85] H. Asayesh-Ardakani, W. Yao, Y. Yuan, A. Nie, K. Amine, J. Lu, R. Shahbazian-Yassar, *Small Methods* **2017**, *1*, 1700202.

[86] K. E. Gregorczyk, Y. Liu, J. P. Sullivan, G. W. Rubloff, *ACS Nano* **2013**, *7*, 6354.

[87] G. R. Love, *Acta Metall*. **1964**, *12*, 731.

[88] J. Huang, M. Meyer, V. Pontikis, *Phys. Rev. Lett*. **1989**, *63*, 628.

[89] J. Rabier, M. P. Puls, *Philos. Mag. A* **1989**, *59*, 533.

[90] P. Shewmon, *Diffusion in solids*, Springer, Switzerland **2016**.

[91] S. Zhang, *npj Comput. Mater*. **2017**, *3*, 1.

[92] J. L. Goldman, B. R. Long, A. A. Gewirth, R. G. Nuzzo, *Adv. Funct. Mater*. **2011**, *21*, 2412.

[93] S. Mirabella, D. De Salvador, E. Napolitani, E. Bruno, F. Priolo, *J. Appl. Phys*. **2013**, *113*, 3.

[94] C. K. Chan, H. Peng, G. Liu, K. McIlwrath, X. F. Zhang, R. A. Huggins, Y. Cui, *Nat. Nanotech*. **2008**, *3*, 31.

[95] X. H. Liu, Y. Liu, A. Kushima, S. Zhang, T. Zhu, J. Li, J. Y. Huang, *Adv. Energy Mater.* **2012**, *2*, 722.

[96] W. Liang, H. Yang, F. Fan, Y. Liu, X. H. Liu, J. Y. Huang, T. Zhu, S. Zhang, *ACS Nano* **2013**, *7*, 3427.

[97] Y.-W. Byeon, J.-P. Ahn, J.-C. Lee, *Small* **2020**, in print.

[98] C. K. Chan, R. N. Patel, M. J. O'connell, B. A. Korgel, Y. Cui, *ACS Nano* **2010**, *4*, 1443.

[99] Q. Xiao, M. Gu, H. Yang, B. Li, C. Zhang, Y. Liu, F. Liu, F. Dai, L. Yang, Z. Liu, *Nat. Commun.* **2015**, *6*, 1.

[100] J. Cho, *J. Mater. Chem.* **2010**, *20*, 4009.

[101] Z. Jia, T. Li, *J. Power Sources* **2015**, *275*, 866.

[102] D. Bresser, S. Passerini, B. Scrosati, *Energy Environ. Sci.* **2016**, *9*, 3348.

[103] N. Nitta, G. Yushin, *Part. Part. Syst. Charact.* **2014**, *31*, 317.

[104] M. R. Palacin, *Chem. Soc. Rev.* **2009**, *38*, 2565.

[105] M.-G. Park, G.-K. Sung, N.-E. Sung, J.-H. Kim, C.-M. Park, *J. Power Sources* **2016**, *328*, 607.

[106] S. Böhme, K. Edström, L. Nyholm, *Electrochim. Acta* **2015**, *179*, 482.

[107] P. Lian, X. Zhu, S. Liang, Z. Li, W. Yang, H. Wang, *Electrochim. Acta* **2011**, *56*, 4532.

[108] M.-K. Kim, S.-H. Yu, A. Jin, J. Kim, I.-H. Ko, K.-S. Lee, J. Mun, Y.-E. Sung, *Chem. Commun.* **2016**, *52*, 11775.

[109] Y.-T. Cheng, M. W. Verbrugge, *J. Power Sources* **2009**, *190*, 453.

[110] C. Heubner, M. Schneider, A. Michaelis, *Adv. Energy Mater.* **2020**, *10*, 1902523.

[111] B. Byles, N. Palapati, A. Subramanian, E. Pomerantseva, *APL Mater.* **2016**, *4*, 046108.

[112] G. Pekar, A. Singaevsky, *Mater. Sci. Semicond. Process.* **2017**, *64*, 10.

[113] N. Ding, J. Xu, Y. Yao, G. Wegner, X. Fang, C. Chen, I. Lieberwirth, *Solid State Ion*. **2009**, *180*, 222.

[114] L. Baggetto, P. Ganesh, C.-N. Sun, R. A. Meisner, T. A. Zawodzinski, G. M. Veith, *J. Mater. Chem. A* **2013**, *1*, 7985.

[115] Y.-S. Choi, Y.-W. Byeon, J.-P. Ahn, J.-C. Lee, *J. Mater. Chem. A* **2018**, *6*, 9428.

[116] V. Viswanathan, J. Nørskov, A. Speidel, R. Scheffler, S. Gowda, A. Luntz, *J. Phys. Chem. Lett*. **2013**, *4*, 556.

[117] Y.-S. Choi, J.-C. Lee, *J. Mater. Chem. A* **2018**, *6*, 11531.

[118] P. Biswal, S. Stalin, A. Kludze, S. Choudhury, L. A. Archer, *Nano Lett*. **2019**, *19*, 8191.

[119] Y. He, X. Ren, Y. Xu, M. H. Engelhard, X. Li, J. Xiao, J. Liu, J.-G. Zhang, W. Xu, C. Wang, *Nat. Nanotech*. **2019**, *14*, 1042.

[120] L. Benitez, J. M. Seminario, *J. Electrochem. Soc*. **2017**, *164*, E3159.

[121] J. Qian, W. A. Henderson, W. Xu, P. Bhattacharya, M. Engelhard, O. Borodin, J.-G. Zhang, *Nat. Commun*. **2015**, *6*, 1.

[122] M. D. Tikekar, S. Choudhury, Z. Tu, L. A. Archer, *Nat. Energy* **2016**, *1*, 1.

[123] X. Wang, L. Fan, D. Gong, J. Zhu, Q. Zhang, B. Lu, *Adv. Funct. Mater*. **2016**, *26*, 1104.

[124] W. Liu, P. Liu, D. Mitlin, *Adv. Energy Mater*. **2020**, *10*, 2002297.

[125] J.-H. Park, Y.-S. Choi, H.-J. Lee, H.-C. Shim, J.-P. Ahn, J.-C. Lee, *Nano Lett*. **2019**, *19*, 3692.

[126] G. Singh, B. Acebedo, M. C. Cabanas, D. Shanmukaraj, M. Armand, T. Rojo, *Electrochem. Commun*. **2013**, *37*, 61.

[127] K. Kubota, S. Komaba, *J. Electrochem. Soc*. **2015**, *162*, A2538.

[128] S. Komaba, T. Ishikawa, N. Yabuuchi, W. Murata, A. Ito, Y. Ohsawa, *ACS Appl. Mater. Inter.* **2011**, *3*, 4165.

[129] S. Menkin, D. Golodnitsky, E. Peled, *Electrochem. Commun.* **2009**, *11*, 1789.